

Raman microprobe characterization of electrodeposited S-rich $\text{CuIn}(\text{S},\text{Se})_2$ for photovoltaic applications: Microstructural analysis

V. Izquierdo-Roca, A. Pérez-Rodríguez,^{a)} A. Romano-Rodríguez, and J. R. Morante
Lab. Enginyeria i Materials Electrònics (EME), Institut de Nanociència i Nanotecnologia de la Universitat de Barcelona (IN²UB), C. Martí i Franqués 1, 08028 Barcelona, Spain

J. Álvarez-García
Centre de Recerca i Investigació de Catalunya (CRIC), Trav. de Gràcia 108, 08012 Barcelona, Spain

L. Calvo-Barrio
Lab. Anàlisis de Superfícies, Serveis Científic-Tècnics (SCT), Univ. Barcelona, C. Lluís Solé i Sabarís 1-3, 08028 Barcelona, Spain

V. Bermudez, P. P. Grand, O. Ramdani, L. Parissi, and O. Kerrec
IRDEP, Institute of Research and Development of Photovoltaic Energy (UMR 7174, CNRS/EDF/ENSCP), 6 Quai Watier, BP 49, 78401 Chatou cedex, France

(Received 13 February 2007; accepted 20 March 2007; published online 22 May 2007)

This article reports a detailed Raman scattering and microstructural characterization of S-rich $\text{CuIn}(\text{S},\text{Se})_2$ absorbers produced by electrodeposition of nanocrystalline CuInSe_2 precursors and subsequent reactive annealing under sulfurizing conditions. Surface and in-depth resolved Raman microprobe measurements have been correlated with the analysis of the layers by optical and scanning electron microscopy, x-ray diffraction, and in-depth Auger electron spectroscopy. This has allowed corroboration of the high crystalline quality of the sulfurized layers. The sulfurizing conditions used also lead to the formation of a relatively thick MoS_2 intermediate layer between the absorber and the Mo back contact. The analysis of the absorbers has also allowed identification of the presence of In-rich secondary phases, which are likely related to the coexistence in the electrodeposited precursors of ordered vacancy compound domains with the main chalcopyrite phase, in spite of the Cu-rich conditions used in the growth. This points out the higher complexity of the electrodeposition and sulfurization processes in relation to those based in vacuum deposition techniques. © 2007 American Institute of Physics. [DOI: [10.1063/1.2734103](https://doi.org/10.1063/1.2734103)]

I. INTRODUCTION

Cu-based chalcopyrite materials ($\text{Cu-B}^{\text{III}}\text{-C}_2^{\text{VI}}$) have become a competitive alternative for the production of photovoltaic cells. These materials have adequate optoelectronic properties, and band gaps well matched to the solar spectrum. Furthermore, their chemical structure allows triggering of their optical properties within a wide range by means of introducing an adequate substitutional atom into the crystallographic structure. Up to now, optimum results in terms of efficiency have been obtained by using a complex alloy $\text{Cu}(\text{In},\text{Ga})(\text{S},\text{Se})_2$ as absorber layer, which renders efficiencies above 19%.¹ Nevertheless, a deeper understanding of the properties of this material and the film formation mechanisms is still necessary in order to improve the efficiency and competitiveness of chalcopyrite-based solar cell technologies.

In this article, we present a detailed Raman scattering and microstructural characterization of S-rich $\text{CuIn}(\text{S},\text{Se})_2$ absorbers produced by a two-step process involving the electrodeposition of a nanocrystalline CuInSe_2 precursor and a subsequent reactive annealing under sulfurizing conditions. This technology has a huge market potential, since it re-

places several vacuum sputtering deposition processes, which are usually required to produce good-quality absorbers, with a single electrodeposition step.² Exploitation of the simplicity, low-cost process capability, and scalability to industrial production characteristic of the electrodeposition processes will allow significant cost reduction to be obtained in relation to the costs of nowadays standard thin-film solar cell technologies. Solar cell efficiencies up to 11% have already been reported for devices fabricated according to this two-step electrodeposition and sulfurization process.³ These efficiencies are close to that achieved in CuInS_2 -based devices synthesized using standard vacuum deposition processes.⁴ Nevertheless, and despite the work carried out in the last two decades, electrodeposition of chalcopyrite semiconducting compounds is still a relatively unknown process. A more detailed and better knowledge of the morphological and physico-chemical properties of these films is strongly required in order to optimize the film properties, and the absorber manufacturing technology.

Raman scattering constitutes a technique well suited for the microstructural characterization of chalcopyrite-based processes. The zone center phonon representation of the chalcopyrite structure is constituted by 21 optical modes, of which only the two A_2 modes are silent,

^{a)}Electronic mail: perez-ro@el.ub.es

$$\Gamma = A_1 \oplus 2A_2 \oplus 3B_1 \oplus 3B_2^{(LO,TO)} \oplus 6E^{(LO,TO)}.$$

Chalcopyrite modes are grouped into three frequency bands (low, central, and high energy bands), which can be interpreted as arising from the Γ , X , and W points of the Brillouin zone of the zinc-blende analogous pseudobinary compound.⁵ Most of these modes have a very low scattering cross section and overlap each other, and thus are difficult to resolve even at low temperature using polarization configurations. The A_1 symmetry mode, corresponding to the antiphase vibration of the anions in the lattice, constitutes the most remarkable exception, and it is usually the most intense band in the spectra of chalcopyrite compounds. In addition, it has been demonstrated that the spectral properties of this band in photovoltaic absorbers are closely linked to the crystalline quality of the layer, and to the solar efficiency of the final device.^{6,7}

In order to deep in the crystalline and microstructural characterization of the layers, surface and in-depth resolved Raman microprobe measurements have been correlated with the analysis of the layers by optical and scanning electron microscopy, x-ray diffraction, and in-depth Auger electron spectroscopy. All these measurements have allowed us to identify the main and secondary phases present in the absorbers and the dependence of their main microstructural features on the different process steps. This analysis has revealed the existence of significant differences in relation to the much better known vacuum deposition processes, which point out the higher complexity of the mechanisms involved in the synthesis and recrystallization of the electrodeposited absorbers.

II. EXPERIMENT

S-rich $\text{CuIn}(\text{S,Se})_2$ absorbers have been produced onto Mo-coated glass using a two-step process. First, a nanocrystalline CuInSe_2 precursor layer was obtained by means of one-step electrodeposition in an acidic bath containing Cu^{2+} , In^{3+} , and H_2SeO_3 electroactive species. The electrodeposition conditions were chosen in order to produce films with overall stoichiometry given by $\text{In}/\text{Cu}=0.9$ and $\text{Se}/(\text{Cu}+\text{In})=1.2$. After electrodeposition, the films were annealed in a sulfur-containing atmosphere using a rapid thermal process (RTP). After the sulfurization reaction, the absorbers were treated in a NaCN bath in order to etch the surface Cu-rich phases related to segregation of Cu excess in the surface of the films.

Nanocrystalline precursor layers and polycrystalline sulfurized absorbers (before and after NaCN etching) were characterized by means of Raman spectroscopy (RS) in combination with optical microscopy (OM), scanning electron microscopy (SEM), x-ray diffraction (XRD), and Auger electron spectroscopy (AES). Raman microprobe measurements were performed using a T64000 Jobin-Yvon spectrometer coupled to an Olympus metallographic microscope. Excitation was provided with the 514.5 nm emission line of an Ar^+ laser and measurements were performed in backscattering configuration. Measurements on as-grown electrodeposited samples were made using the $\times 50$ (NA 0.55) objective of the optical microscope, which gives a laser spot on the surface of the sample with an estimated size of about $1.2 \mu\text{m}$, with a

penetration depth of about 100 nm. For the annealed samples, submicronic spatial resolution was obtained using the $\times 100$ (NA 0.95) objective of the microscope. This has allowed performance of preliminary in-depth measurements by directly focusing the light spot at different depths in the cross section of the samples. In all cases, power on the sample was 0.5 mW, which corresponds to power densities of $50 \text{ kW}/\text{cm}^2$ ($\times 50$ objective) and $150 \text{ kW}/\text{cm}^2$ ($\times 100$ objective), respectively. For these power conditions, no observable thermal effects on the Raman spectra were found. This configuration also allows one to obtain OM images by coupling the microscope output to a 640×480 charge-coupled device (CCD).

A Hitachi S-4100 scanning electron microscope was used in order to investigate the nanostructure and morphology of the layers. In-depth chemical compositional profiles of the sulfurized layers were obtained by means of AES, using a Phi 670 scanning Auger nanoprobe. The electron gun parameters selected for the measurements were electron beam energy 10 keV, and filament current 10 nA. The scanned area for the AES measurements was about $10 \times 10 \mu\text{m}^2$, for a focused beam diameter below 100 nm. For the in-depth measurements, ion sputtering was carried out with an Ar^+ beam with energy below 5 keV in order to avoid inducing significant damage. For the sulfurized and NaCN etched samples, in order to obtain quantitative Auger results AES measurements have been performed in standards of CuInS_2 and MoS_2 . These data have allowed calibration of the sensitivity factors used in the quantitative calculations.⁸ The accuracy obtained by using standard samples is about 5% in absolute elemental concentration.

Furthermore, in order to deepen the in-depth resolved analysis of the layers, combined in-depth Raman/AES measurements were also performed by acquiring sequentially a series of Raman spectra after sputtering the sample in the AES system between every Raman measurement. Since the penetration depth of the green light in $\text{CuIn}(\text{S,Se})_2$ is only around 100 nm, this procedure allows one to obtain complete information on the bulk of the films. A detailed description of this combined technique can be found elsewhere.⁹

Finally, $2\theta/\theta$ XRD measurements were done in a Philips MRS diffractometer and Ω -scan XRD measurements were done in a Siemens D-500 diffractometer, using the $K\alpha$ emission line of copper.

III. RESULTS AND DISCUSSION

A. Electrodeposited as-grown layers

Electrodeposited CuInSe_2 films are characterized by nonuniform chemical, structural, and morphological properties. Cross-section SEM images [Fig. 1 (left)] reveal that the samples are constituted by a $1.6 \mu\text{m}$ thick CuInSe_2 layer, presenting a vertical columnar structure. The layer is also characterized by the presence of vertical pores [indicated with arrows in Fig. 1 (left)] that extend from the surface down to the midregion in the layers. At the back region, there is an improvement in the layer compactness. The $\text{CuInSe}_2/\text{Mo}$ interface appears to be free of voids, thus ensuring good electrical contact and film adherence. Further-

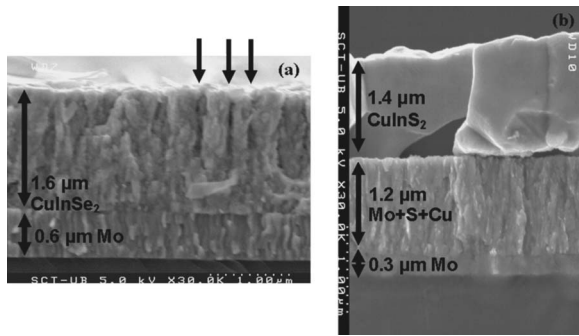


FIG. 1. SEM cross-section view of (left) as-grown electrodeposited precursor and (right) sulfurized and NaCN etched absorber.

more, planar view images show the presence of surface inhomogeneities which are also visible in the OM images (as will be shown later). According to the results of the microstructural analysis presented below, these inhomogeneities have been related to surface segregation of CuSe and Se crystals. Average grain size inferred from SEM images is in the range of 50 nm.

Surface Raman spectra of the precursor layers are characterized by the presence of fingerprint bands of chalcopyrite ordered CuInSe₂, as shown in Fig. 2. The most characteristic chalcopyrite band appears at 175 cm⁻¹, and corresponds to the A₁ mode within the central energy band (173–216 cm⁻¹). This central energy band groups four additional modes ($B_1^{(2)} \oplus B_2^{(2)} \oplus 2E^{(3,4)}$), which are hindered in the form of a wide spectral contribution. The main peak at 175 cm⁻¹ is blueshifted in relation to the chalcopyrite CuInSe₂ A₁ mode (173 cm⁻¹).⁷ This suggests the presence of a compressive residual stress in the layer. Likewise, the high-energy chalcopyrite band (211–233 cm⁻¹) comprises four modes ($B_1^{(3)} \oplus B_2^{(3)} \oplus 2E^{(5,6)}$), which are especially difficult to resolve due to the nanocrystalline character of the layer, and due to the presence of additional bands arising from the presence of secondary phases. Within the low-frequency chalcopyrite phonon band (60–80 cm⁻¹), in which four modes $B_1^{(1)} \oplus B_2^{(1)} \oplus 2E^{(1,2)}$ lie, only the lowest frequency E⁽¹⁾ mode reported at 60(TO)/61(LO) cm⁻¹ can be clearly distinguished.¹⁰

Note that the full width at half maximum (FWHM) of the A₁ mode is more than five times larger than that of a CuInSe₂ single crystal, thus indicating the poor crystalline quality of the layer. In addition, the presence of a low-frequency shoulder in the 154 cm⁻¹ region is related to the

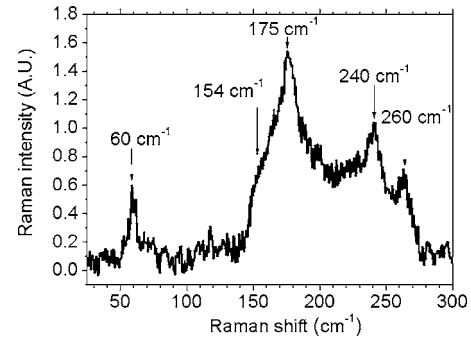


FIG. 2. Surface Raman spectrum of an electrodeposited CuInSe₂ precursor layer.

existence of complex point defects in the chalcopyrite structure (such as $2V_{\text{Cu}} + V_{\text{Se}}$), which give rise to the formation of ordered vacancies compounds (OVCs). These compounds have been reported in the literature to retain a chalcopyrite-related structure, while they are able to accommodate different types of complex defects. Their Raman spectrum is characterized by a strong redshift of the A₁ mode with respect to the vacancy-free chalcopyrite crystal, which is caused by the missing bonds in the OVC structure. The energy of the A₁ mode depends on the final stoichiometry of the OVC,¹¹ being 154 cm⁻¹ for CuIn₃Se₅.¹²

On the other hand, it is evident that the film stoichiometry of the investigated precursors requires a mechanism to accommodate the Cu and Se excess in the film. This mechanism consists of the formation of elemental Se and Cu-Se binary phases, as can be inferred from the analysis of the Raman spectra. The spectra present two peaks at 240 and 261 cm⁻¹. The peak at 240 cm⁻¹ is attributed to the presence of trigonal elementary selenium (Se),¹³ while the peak at 261 cm⁻¹ is characteristic of Cu-Se compounds. The absence of intense low-frequency bands at 17 and 42 cm⁻¹ characteristic of the covellite-type structure (CuSe),¹⁴ and the analysis of the XRD spectra, points to a different binary, probably Cu₂Se, though the coexistence of the covellite CuSe phase cannot be discarded.

Figure 3 (left) shows an OM image of the surface of the as-grown sample. As already indicated, this image shows the presence of surface inhomogeneities that appear as regions with dark contrast. The micro-RS analysis of these surface inhomogeneities shows a strong increase in the intensity of the vibrational modes related to both Se and Cu-Se phases, together with the appearance of an intense contribution at

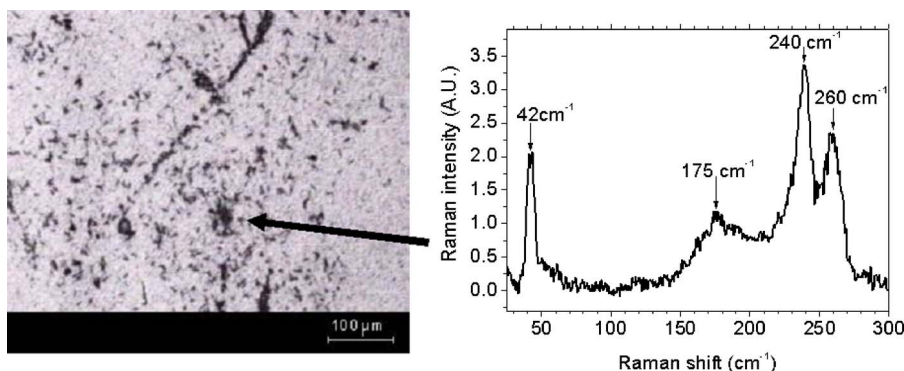


FIG. 3. (left) OM image of a CuInSe₂ precursor, and (right) micro-Raman spectrum measured with the laser spot focused on a dark-surface inhomogeneity.

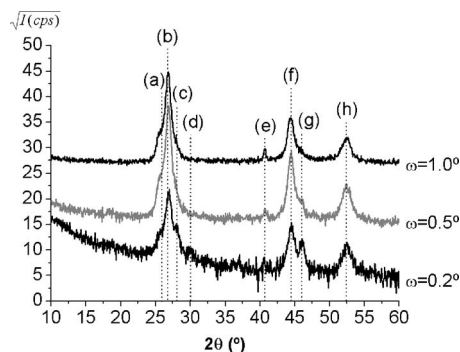


FIG. 4. Grazing incidence XRD diffractograms measured at different values of ω from a CuInSe_2 electrodeposited film. Dashed lines indicate the position of reflections from: (a) CuSe (101), Cu_2Se (222); (b) CuInSe_2 (112); (c) CuSe (102); (d) Se (102); (e) Mo (110); (f) CuInSe_2 (220)/(204), Cu_2Se (404); (g) CuSe (110), and (h) CuInSe_2 (312).

42 cm^{-1} , as can be seen in Fig. 3 (right). This gives clear evidence of the presence in these inclusions of the covellite CuSe phase, revealing the formation at the surface of the layers of Se and CuSe crystalline inclusions.

The formation of these secondary phases is in fact expected under the selected electrodeposition conditions.² However, the appearance of OVC phases in the film clearly shows the complexity of the electrodeposition process. In the present case, the Cu and Se excess conditions favor the nucleation of Se , Cu_2Se , and CuSe nanocrystallites. Once nucleated, their growth likely induces a local deficiency of Se and Cu atoms, which results in the formation of OVC domains within the chalcopyrite CuInSe_2 crystalline grains. The introduction of V_{Cu} and V_{Se} defects in the lattice allows the electric valence of the $\text{Cu}^{(1+)}$, $\text{In}^{(3+)}$, and $\text{Se}^{(2-)}$ atoms in the lattice to be preserved, and ensures the chemical stability of the compound. On the other hand, we note the existence of a film aging process that is characterized by an increase of the Se and CuSe inclusions located at the film surface. Room temperature recrystallization of these secondary phases is responsible for this film aging. Nanometric CuSe/Se grains at the film surface likely act as nucleation grains. Crystal growth could be assisted by the redissolution of energetically metastable nanometric bulk crystallites, and by the grain boundary diffusion toward the film surface. Further investigations are required to fully understand this behavior, which gives another clear indication of the complexity of the electrodeposition process.

The spectra obtained do not allow ruling out the existence of a Cu-Au ordered CuInSe_2 phase (which is characterized by an A_1 mode at 183 cm^{-1}), though it can be stated that, in any case, it is not a dominant phase in the film. Despite the fact that the formation of this metastable phase is known to be favored by low-temperature processing conditions and stoichiometric deviations during film formation,^{11,15} the electrodeposition process do not seem to promote the formation of Cu-Au ordering, while clearly induces the formation of OVCs, even though the overall film stoichiometry is copper rich.

XRD analysis of electrodeposited samples supports the conclusions previously presented (see the spectra in Fig. 4). Detailed analysis of the spectra show the poor quality of the

chalcopyrite phase, as indicated by the broadening of the reflection peaks, and by the absence of the characteristic tetragonal splitting (220)/(204). In addition to chalcopyrite reflections, the spectra show reflections corresponding to the Mo substrate (with low intensity under the selected grazing incidence conditions) and to Se , Cu_2Se , and CuSe secondary phases in the films. Grazing incidence XRD spectra at different ω values reveal that Se and CuSe secondary phases tend to accumulate at the surface of the film, as pointed out by a greater relative contribution of the corresponding reflections. This agrees with the formation of Se and Cu-Se surface aggregates observed from the micro-RS analysis of surface of the samples.

B. Sulfur annealed films

Sulfurization of the precursor layers leads to important modifications in the morphology, composition, and chemical structure of the layers. This can be clearly seen in the cross-section SEM image in Fig. 1 (right), which corresponds to a sulfurized and NaCN etched sample. SEM observations show the formation of large crystals ($1\text{--}2\text{ }\mu\text{m}$ in size), which constitute a major part of the layer. Moreover, the sulfurization process also affects significantly the Mo back contact, giving rise to the formation of an intermediate layer with a thickness of about $1\text{ }\mu\text{m}$. As it will be shown later on, the main phase constituting this layer corresponds to MoS_2 . In principle, the presence of a MoS_2 interface layer between the absorber and the back Mo contact is necessary from the point of view of the solar cell performance, since it avoids the formation of a rectifying junction in the back contact of the cell, allowing for an ohmic one. However, the relatively high thickness of this sulfurized region constitutes a potential source of series resistance losses that could limit the device performance. In this sense, it is important to take into account that the sulfurization step leads to a significantly thinning (in more than 50% of the original thickness) of the Mo back contact layer.

The large grain size of the sulfurized films allows easy determination of the chemical composition of the sample by means of micro-RS. Figure 5 shows the OM image of the surface of the sulfurized layer before NaCN etching, together with the Raman spectra obtained at different points. Dark spots in the OM images present Raman spectra characteristic of a Cu(S,Se) alloy. In this alloy, the A_{1g} mode of the covellite phase of CuS and CuSe binaries gives rise to three different peaks in the spectra, corresponding to the S-S , S-Se , and Se-Se vibrations from the anions located at the $4e$ sites in the covellite structure.¹⁴ Taking into account the experimental dependence of the intensity of the peaks, these spectra indicate a S-rich composition of the Cu(S,Se) alloy, with more than 70% of S atoms at $4e$ sites (which correspond to 2/3 of the total anion sites). On the other hand, spectra obtained from lower contrast areas in the OM image correspond to a pure chalcopyrite phase. The stoichiometry of this phase can also be inferred by analyzing the spectral characteristics of the A_1 mode. In this case, the A_1 mode of the CuIn(S,Se)_2 quaternary presents a bimodal behavior, with two bands involving pure S-S and Se-Se vibrations.¹⁶ As

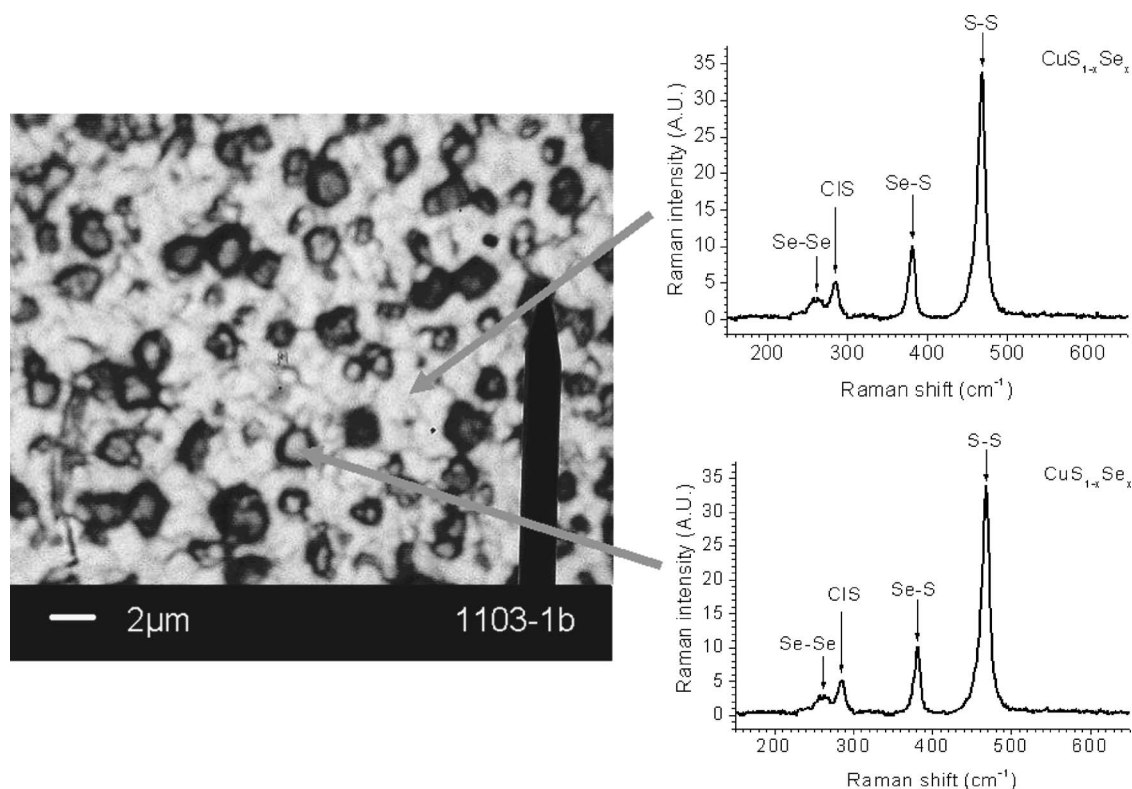


FIG. 5. Micro-Raman spectra obtained with the laser spot focused in two different regions of the surface of a sulfurized precursor. The figure also shows the OM image of the surface of the sample.

shown in Fig. 5, the Raman spectra are characterized by a dominant peak corresponding to the S-S vibrational mode, which indicates that S atoms have almost totally replaced the Se atoms in the crystalline lattice of the chalcopyrite phase, the percentage of remaining Se atoms being of the order of $x \leq 5\%$. On the other hand, it is interesting that the narrower Raman bands in the spectra of these samples also indicate a considerable improvement on their crystalline quality after the sulfurization process, in agreement with the SEM observations.

The cross-section SEM images of these samples show the presence of inclusions in the grain boundaries of the chalcopyrite grains, which are attributed to the Cu(S,Se) crystals (indicated with arrows in Fig. 6). As can be appreciated, these inclusions are not localized only at the surface of the samples, as it is usually found in the sulfurization of metallic precursor layers, but tend to penetrate down the absorber layer through the grain boundary. In some regions (not shown in Fig. 6) Cu(S,Se) crystallites can also be observed close to the interface with the MoS₂ region, although the majority of these aggregates forms at the surface region. This morphology suggests that the sulfurization reaction is not able to promote the segregation of the Cu excess to the surface of the film, but just leads to a chemical and morphological modification of the binary phases already formed during the precursor formation.

The RS analysis of the samples after NaCN etching demonstrates that this process effectively removes these Cu(S,Se) aggregates. Despite the contrasts observed in the OM images from the surface of the etched samples (see Fig. 7), dark areas are associated with surface roughness, as cor-

roborated by micro-RS. This roughness is related to the etching of the Cu(S,Se) inclusions penetrating into the surface region of the absorber layer.

Figure 8 (left) shows the series of Raman spectra measured with the laser spot focused at different positions in the cross section of the etched sample, from the surface region (spectrum¹) to the interface with the back Mo contact layer (spectrum⁴). These measurements have allowed clear experimental evidence to be obtained regarding the formation with

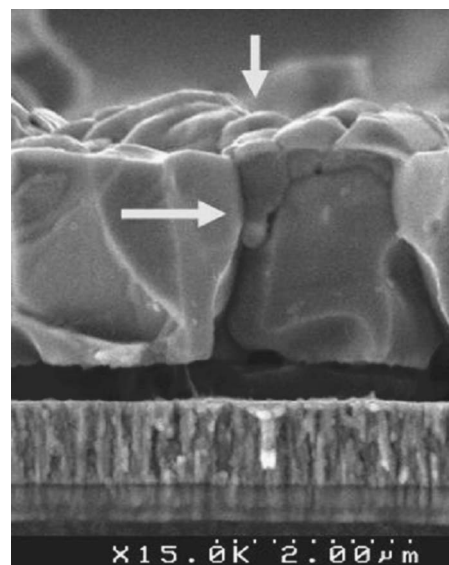


FIG. 6. Detail of a cross-section SEM image from a sulfurized (not etched) sample, showing a Cu(S,Se) surface aggregate (marked with arrows).

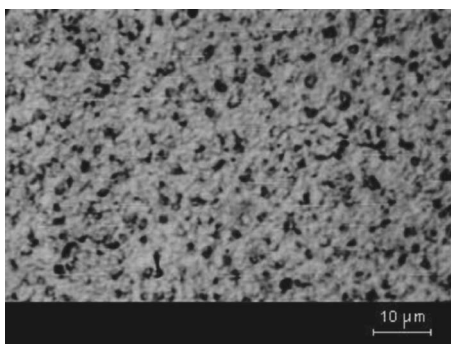


FIG. 7. OM image of the surface of a sulfurized absorber, after etching in NaCN.

the sulfurization process of a MoS_2 region below the absorber layer. As shown in the figure, the spectra measured with the laser spot in this region have two dominant peaks at 377 and 404 cm^{-1} , which agree with the main vibrational modes reported for MoS_2 .¹⁵ In addition, it is possible to observe some weak spectral contributions related to the presence of $\text{Cu}(\text{S,Se})$ inclusions. This can be seen in Fig. 8 (right), which corresponds to the spectrum measured with the laser spot centered at the MoS_2 region [spectrum³ in Fig. 8 (left)]. These contributions are located at 270 and 372 cm^{-1} , the last one appearing as a shoulder at the low-frequency side of the 377 cm^{-1} MoS_2 mode, and correspond to the Se–Se and S–S bands of the A_{1g} vibration of the covellite structure. The correlation observed between the intensity of these weak modes and that of the intense MoS_2 ones suggests that traces of the $\text{Cu}(\text{S,Se})$ phase are located at the intermediate MoS_2 region.

To deepen the in-depth microstructural analysis of these samples, combined Raman/AES measurements have also been performed in the NaCN etched absorber layers. Figure 9 shows the AES compositional depth profiles, as obtained from the spectra corresponding to the main constituents identified in these samples (S, Cu, In, and Mo), as well as the Raman spectra obtained after different sputtering steps.

The AES profiles presented in Fig. 9 show that after the chemical etching, the composition of the absorber layer is close to stoichiometric CuInS_2 but slightly Cu poor, despite the fact that the precursor was grown under Cu excess conditions. Furthermore, the Raman spectra from the bulk of the absorber layer show the presence of a broad contribution in the $320\text{--}360\text{ cm}^{-1}$ spectral range, which can be related to CuIn_3S_8 domains.¹⁷ The presence of this In-rich secondary

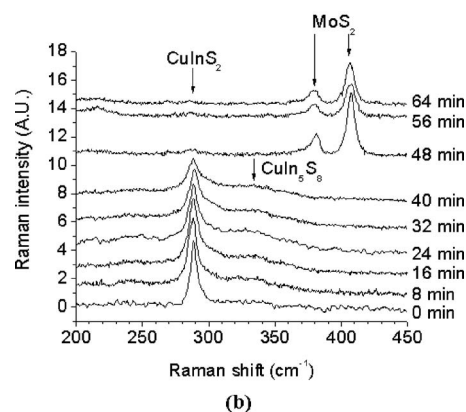
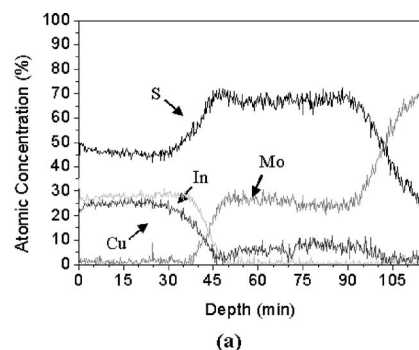


FIG. 9. (a) AES depth profile, and (b) Raman spectra obtained at different depths from a sulfurized and NaCN etched absorber.

phase is in agreement with the slightly Cu-poor composition of the layer. The spectra measured at different sputter times also confirm the existence of an abrupt transition between the absorber layer (up to 40 min of sputter time) and the MoS_2 region (sputter times between 48 and 90 min), these last spectra characterized by the main MoS_2 vibrational modes. According to the AES profiles, the main chemical constituents of this region are Mo and S, which agrees with the identification of MoS_2 as the main phase in this region. Another feature of interest is the penetration of the Cu profile into this region, the estimated Cu content being in the range $5\text{--}10\%$. This supports the assignment of the weak $\text{Cu}(\text{S,Se})$ modes in the spectra directly measured on the cross section of the samples with the presence of traces of this secondary phase in the MoS_2 intermediate region.

The structural analysis of the absorbers has been completed with XRD $2\theta/\theta$ measurements (see Fig. 10). The XRD spectra also show a drastic improvement in the crystalline quality of the chalcopyrite phase, with it now possible

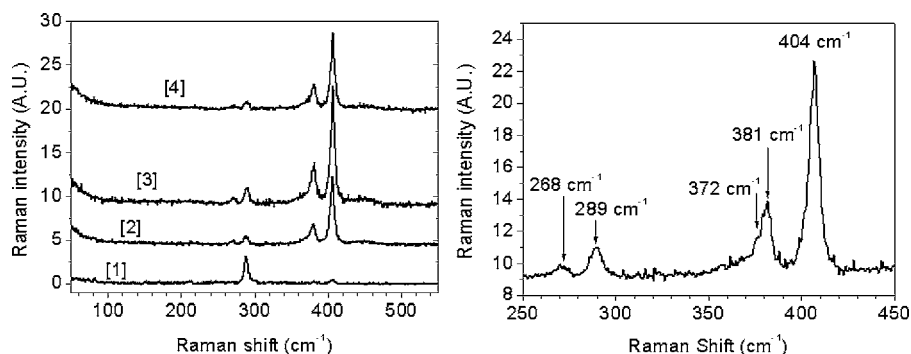


FIG. 8. (Left) Cross-section Raman spectra of a sulfurized and NaCN etched absorber obtained from different positions in the sample. The number of the spectrum increases toward the Mo interface. (Right) Detail of a cross-section spectrum showing the presence of bands indicating the existence of traces of $\text{Cu}(\text{S,Se})$ even after the NaCN etching.

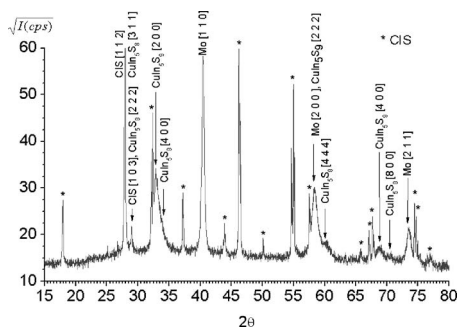


FIG. 10. XRD $2\theta/\theta$ spectrum of a sulfurized and NaCN etched precursor. Peaks related to CuIn_5S_8 are indicated with asterisks. The asymmetric peak at about 33° can be interpreted as due to the contribution in the spectrum of CuIn_5S_9 (200) and CuIn_5S_8 (400) reflections (Refs. 18 and 19). The spectrum also shows peaks that can be indexed with CuIn_5S_9 (400) (at about 69°), CuIn_5S_8 (444) (at about 60.1°), and CuIn_5S_8 (800) (at about 70.7°).

to resolve the characteristic tetragonal splitting in the peaks (200)/(004), (220)/(204), etc. In addition, weak reflections appear in the spectrum, which cannot be indexed according to either the chalcopyrite or the Mo substrate diffraction patterns. Most of such reflections can be interpreted with the diffraction pattern of the CuIn_5S_8 spinel, thus supporting the in-depth Raman observations. Moreover, a second group of weak peaks could be indexed as (200) and (400) of the CuIn_5S_9 compound.^{18,19} No other diffractogram in the JCPDS could explain these reflections.

These results point to the existence of significant differences in the microstructural evolution of the electrodeposited and sulfurized layers in relation to the behavior of films synthesized using vacuum deposition processes. These are related to the absence of a significant contribution of Cu–Au metastable domains in the spectra from the annealed layers, in spite of the In-rich secondary phases present in the absorbers and their final Cu-poor composition. For samples obtained using vacuum deposition processes such as coevaporation, the presence of these secondary phases is accompanied by a degradation of the microstructural quality of the absorbers, concomitant with the existence of CuAu metastable ordered microcrystalline domains.^{6,7}

On the other hand, the final Cu-poor composition of the sulfurized layers is likely related to the presence of OVC Cu-poor domains in the CuInSe_2 precursors, in spite of the Cu and Se excess conditions during their electrochemical growth. These results suggest the existence of a direct relationship between the final microstructure of the sulfurized layers and the binary and ternary phases present in the electrochemically grown nanocrystalline precursor.

IV. CONCLUSIONS

This work describes the detailed Raman scattering and microstructural characterization of S-rich $\text{CuIn}(\text{S},\text{Se})_2$ photovoltaic absorbers produced by sulfurization of electrodeposited CuInSe_2 precursors.

Electrodeposited layers are mainly constituted by nanocrystalline CuInSe_2 grains with chalcopyrite structure. Elemental Se, CuSe, and Cu_2Se are the most significant secondary phases present in the precursors. Despite the selected Cu and Se excess growth conditions, the Raman spectra from

these samples also reveal the presence of OVC domains. The sulfurization process leads to a significant improvement of the crystalline quality of the chalcopyrite phase, as well to an increase of the average crystal size.

The high microcrystalline quality of the synthesized precursors is responsible for the high efficiency reported for solar cells fabricated with these absorbers. This contrasts with the Cu-poor composition of the absorber, which is likely related to the coexistence of Cu-poor OVC domains with the main chalcopyrite phase in the electrodeposited precursors. This likely results in the formation of secondary In-rich phases such as CuIn_5S_8 and CuIn_5S_9 , though the OVC phase does not seem to persist after the sulfurization reaction. It was observed also that despite the Cu-poor final composition of the absorbers, no trace of CuAu ordering was found in the resulting $\text{CuIn}(\text{S},\text{Se})_2$ phase. Furthermore, the sulfurization process also leads to the formation of a thick intermediate MoS_2 region. The in-depth detailed analysis shows the presence of a significant Cu content in this region, which has been related to the identification of a secondary Cu(S,Se) phase remaining in the final samples. This, together with the high thickness of the MoS_2 region, is a potential source of lowering of the efficiency of the solar cell devices.

To summarize, the investigated growth process is adequate to produce good-quality chalcopyrite $\text{CuIn}(\text{S},\text{Se})_2$ absorbers. Even though the resulting layers are free of Cu–Au ordered phase, the presence of which has been previously related to the degradation of the optoelectronic properties of photovoltaic absorbers, the coexistence of In-rich secondary phases such as CuIn_5S_8 , together with the formation of a thick intermediate MoS_2 region with Cu-rich secondary phases, may limit the performance of these samples in photovoltaic devices.

ACKNOWLEDGMENTS

EME is a member of CERMAE (Centre de Referència en Materials Avançats per a l'Energia) and CEMIC (Centre of Microsystems Engineering) of the "Generalitat de Catalunya". This work was funded by the LARCIS project (SES6-CT-2005-019757) of the 6th FM Programme of the European Commission.

¹B. J. Stanbery, Crit. Rev. Solid State Mater. Sci. **27**, 73 (2002).

²D. Lincot, Thin Solid Films **487**, 40 (2005).

³D. Lincot, J. F. Guillemoles, S. Taunier, D. Guimar, J. Six-Kurdi, A. Chaumont, O. Roussel, O. Ramdani, C. Hubert, J. P. Fauvarque, N. Boderreau, L. Parissi, P. Panheleux, P. Fanouillere, N. Naghavi, P. P. Grand, M. Benfarah, P. Mogensen, and O. Kerrec, Solar Energy **77**, 725 (2004).

⁴R. Klenk, J. Klaer, R. Scheer, M. Ch. Lux-Steiner, I. Luck, N. Meyer, and U. Rühle, Thin Solid Films **480**, 509 (2005).

⁵J. Camassel, L. Artus, and J. Pascual, Phys. Rev. B **41**, 5727 (1990).

⁶J. Álvarez-García, E. Rudigier, N. Regam, B. Barcones, R. Scheer, A. Pérez-Rodríguez, A. Romano-Rodríguez, and J. R. Morante, Thin Solid Films **431–432**, 122 (2003).

⁷J. Álvarez-García, B. Barcones, A. Pérez-Rodríguez, A. Romano-Rodríguez, J. R. Morante, A. Janotti, S.-H. Wei, and R. Scheer, Phys. Rev. B **71**, 054303 (2005).

⁸Handbook of Auger Electron Spectroscopy, edited by C. L. Hedberg (Physical Electronics, Eden Prairie, MN, 1995).

⁹L. Calvo-Barrio, A. Pérez-Rodríguez, J. Álvarez-García, A. Romano-Rodríguez, B. Barcones, J. R. Morante, K. Siemer, I. Luck, R. Klenk, and R. Scheer, Vac. **63**, 315 (2001).

¹⁰H. Tanino, Phys. Rev. B **45**, 13223 (1992).

- ¹¹C.-M. Xu, X.-L. Xu, J. Xu, X.-J. Yang, J. Zuo, N. Kong, W.-H. Huang, and H.-T. Liu, *Semicond. Sci. Technol.* **19**, 1201 (2004).
- ¹²C. Rincón, S. M. Wasim, G. Marín, J. M. Delgado, J. R. Huntzinger, A. Zwick, and J. Gabibert, *Appl. Phys. Lett.* **73**, 441 (1998).
- ¹³O. Ramdani, J. F. Guillemoles, D. Lincot, P. P. Grand, E. Chassaing, O. Kerrec, and E. Rzepka, *Thin Solid Films* **515**, 5909 (2007).
- ¹⁴M. Ishii, K. Shibata, and H. Nozaki, *J. Solid State Chem.* **105**, 504 (1993).
- ¹⁵J. Álvarez-García, A. Pérez-Rodríguez, A. Romano-Rodríguez, J. R. Morante, L. Calvo-Barrio, R. Scheer, and R. Klenk, *J. Vac. Sci. Technol. A* **19**, 232 (2001).
- ¹⁶R. Bacewicz, W. Gebicki, and J. Filipowicz, *J. Phys. Condens. Matter* **6**, L777 (1994).
- ¹⁷N. M. Gasanly, S. A. El-Hamid, L. G. Casanova, and A. Z. Magomedov, *Phys. Status Solidi B* **169**, K115 (1992).
- ¹⁸S. Kobayashi, N. Tsuboi, T. Sega, K. Oishi, and F. Kaneko, *Jpn. J. Appl. Phys., Part 1* **42**, 5485 (2003).
- ¹⁹G. G. Guseinov, I. G. Aliev, S. S. Rzaev, O. M. Aliev, and F. I. Aliev, *Inorg. Mater.* **29**, 538 (1993).